Numerical Simulation of Macrosegregation: a Comparison between Finite Volume Method and Finite Element Method Predictions and a Confrontation with Experiments

N. AHMAD, H. COMBEAU, J.-L. DESBIOLLES, T. JALANTI, G. LESOULT, J. RAPPAZ, M. RAPPAZ, and C. STOMP

Micro-macrosegregation calculations have been performed for a rectangular cavity containing either a Pb-48 wt pct Sn alloy or a Sn-5 wt pct Pb alloy. The numerical results calculated with a finite volume method (FVM) and a finite element method (FEM) are compared with experimental results previously obtained by Hebditch and Hunt.[1] The two methods are based on the same average conservation equations governing heat and mass transfer and the same assumptions: lever rule, equal and constant density of the solid and liquid phases (except in the buoyancy term), permeability of the mushy zone given by the Carman–Kozeny relation, and no transport of the solid phase. Although the same parameters are used in both calculations, small differences are observed as a result of the different formulations. In particular, the instabilities appearing in the mushy zone (channels) of the Sn-5 wt pct Pb alloy are more pronounced with the FVM formulation as compared with FEM, whereas the opposite trend is observed for the Pb-48 wt pct Sn alloy. Nevertheless, the final segregation maps at the end of solidification compare fairly well with the experimental findings.

I. INTRODUCTION

MACROSEGREGATION, *i.e.*, variations of average mass fractions at the macroscopic scale of a casting, plays an important role in many solidification processes. It can be induced by fluid flow in the mushy zone,[2–7] which redistributes segregated solute elements within the remaining liquid volume; by deformation of the solid skeleton in the semisolid state;[8,9] or by transport of equiaxed grains.[10,11,12] The movement of the fluid flow can be associated with thermal and/or solutal buoyancy,[3,4,5] shrinkage,[13,14] or surface exudations.[15] These two last phenomena usually lead to "inverse segregation," *i.e.*, to a solid at the surface of the casting, which is solute rich if the partition coefficient is smaller than unity. Natural convection gives rise to complex segregation maps, which are schematically summarized in Figure 1 for a rectangular cavity and two alloys: Sn-5 wt pct Pb and Pb-48 wt pct Sn.

In this study, the situations where the cavity is cooled from the left lateral side have been considered. At the beginning of solidification, horizontal gradient of temperature and liquid solute mass fraction develop close to the chill. These two gradients lead to a horizontal gradient of the liquid density. As the gravity is perpendicular to this gradient, fluid flow driven by natural convection (both thermal and solutal) appears early during solidification. Since the partition coefficient of the solute of both alloys is smaller than unity, the interdendritic liquid becomes solute rich in both cases as solidification proceeds, *i.e.*, as the temperature goes down. For the tin-rich alloy (Figure 1(a)), this liquid becomes heavier as an effect of the combined thermal and solutal fields and the resulting convection is counterclockwise (ccw). For the lead-rich alloy (Figure 1(b)), the effects of solute and temperature on the liquid density are opposite, but solute-induced convection dominates in this case and a clockwise (cw) vortex will form. When the cavity is cooled down from the bottom surface, stagnant layers of liquid form in the case of the tin-lead alloy (Figure 2(a)), whereas the situation of lead-tin is potentially unstable as the tin-rich interdendritic liquid has a tendency to go up (Figure 2(b)). This can lead to Rayleigh–Bénard cells in a first step or even to freckles (*i.e.*, remelting of small channels in the mushy zone).[16,17,18]

Natural convection induced by the thermal and/or solutal fields and their influence on the solidification path of alloys has been modeled by several authors for more than a decade.[16,19–21] For that purpose, the conservation equations are averaged over a volume element, which is small with respect to the extent of the mushy zone and large with respect to the typical dendrite arm spacing.[6,22–24] This introduces a drag term in the Navier–Stokes equation, similar to that describing the fluid flow in a porous medium.[23] The equations of conservation for heat, mass, momentum, and solute are then solved numerically using, in most cases, the finite volume method (FVM)[20,25–30] or, more occasionally, the finite element method (FEM).[3,16,31,32] Some studies have investigated the influences of microsegregation[2] (*i.e.*, use of a Scheil law instead of a lever rule), of the transport of equiaxed grains in the liquid,[10,14] or of shrinkage.[16,27,33–35] However, no comparison has been made among codes solving the same equations (benchmark test). Therefore, it is unclear how the numerical formulation and the choice of numerical parameters influence the final segregation results, in particular, regarding the channel prediction. The same

N. AHMAD, Postdoctoral Fellow, and J. RAPPAZ, Professor, are with Chaire d'analyse et simulations numériques, Ecole Polytechnique Fédérale de Lausanne, CH-1015 Lausanne, Switzerland. J.-L. DESBIOLLES, Staff Member, T. JALANTI, Ph.D. Student, and M. RAPPAZ, Professor, are with Laboratoire de Métallurgie Physique, Ecole Polytechnique Fédérale de Lausanne, CH-1015 Lausanne, Switzerland. H. COMBEAU, Assistant Professor, G. LESOULT, Professor, and C. STOMP, Postdoctoral Fellow, are with Laboratoire de Science et de Génie des Matériaux Métalliques, INPL, Ecole des Mines de Nancy, F-54042 Nancy, Cedex, France.

Manuscript submitted July 11, 1997.

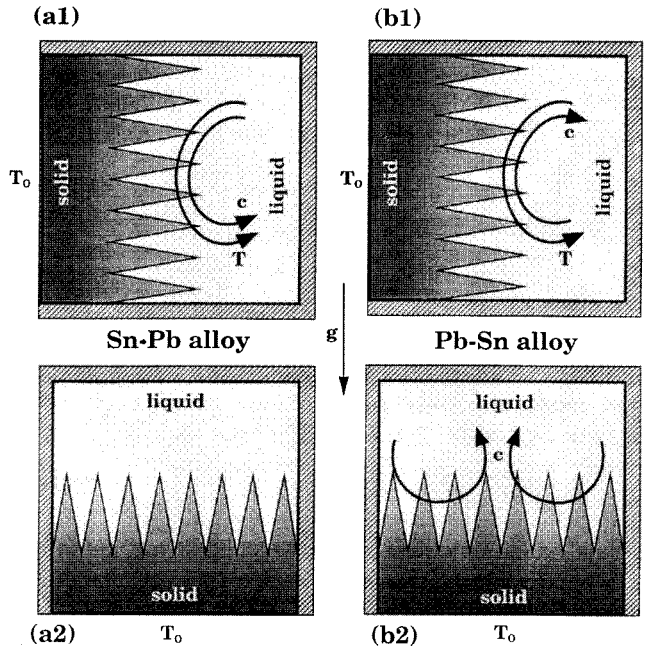

Fig. 1—Schematics of thermosolutal situations encountered with (*a*) Sn-5 wt pct Pb and (*b*) Pb-48 wt pct Sn alloys. In (1), the cavity is cooled from the lateral side and the volumetric mass gradient is primarily horizontal, whereas in (2), it is vertical, since cooling is applied at the bottom of the cavity.

remark can be made for the influence of some parameters such as the secondary dendrite arm spacing (DAS), or permeability, or viscosity. Finally, simulation results have been rarely compared with experimental observations performed under controlled conditions.[36,37,38]

The goal of the present contribution is to make such comparisons. A FVM code,[26,39,40] developed at the Ecole des Mines de Nancy, and a FEM code, 3-MOS,[41,42] developed at the Ecole Polytechnique Fédérale de Lausanne, have been slightly modified so as to solve exactly the same average conservation equations of heat, mass, momentum, and solute. The same underlying assumptions have been made, which include that the densities of the solid and liquid phases are equal and constant, except in the buoyancy term of the momentum equation (Boussinesq's approximation); microsegregation is given by the lever rule; and permeability is calculated with the Carman–Kozeny model. The basic underlying equations and assumptions of the physical model are summarized in Section III. Sections IV and V present the FVM and FEM formulations, respectively. In Section VI, the simulation results obtained with the two numerical codes are compared, and in Section VII, a comparison with experimental results previously reported by Hebditch and Hunt[1] (HH results) is given.

II. HEBDITCH AND HUNT EXPERIMENT

In the HH experiment, two alloys, Pb-48 wt pct Sn and Sn-5 wt pct Pb, have been solidified in a parallelepipedic cavity 6-cm high, 10-cm long, and 1.3-cm thick. This cavity was thermally insulated on all surfaces except for the thinnest lateral surface, which could be water cooled after the alloy was completely melted. Assuming that the fluid flow in the largest midplane section was not influenced by the two parallel walls of the cavity, the situation can be viewed as a two-dimensional rectangular cavity similar to that described at the top of Figure 1. The alloy could be quenched during solidification in order to visualize the advance of the front. The results of HH were presented in the form of segregation maps, which consisted in mass fractions measured at 36 different points in a midplane section of the ingot. As the solidification times and thermal fields were not accurately known or reported in the HH article, the cooling conditions used in the present simulation work had to be estimated. This was done on the basis of the advance of the solidification front as observed by HH at the various times of quench. A constant heat transfer coefficient between the casting and the cooling system was estimated on this basis, the value of which is reported in Table I, together with all the other parameters of the calculations and of the alloys.

III. MODEL

Average conservation equations are used in the present physical model.[6,22–24] The mass, heat, and solute conservation equations are averaged over both the liquid and solid phases, whereas that relative to momentum is averaged only over the liquid phase.[6,23] This naturally introduces a drag force of the solid skeleton on the interdendritic liquid region. Therefore, for a binary alloy, the unknown entities at each node of the enmeshment are the following: the volume fraction of solid, $g_s(\mathbf{x},t)$; the temperature, $T(\mathbf{x},t)$; the average volumetric enthalpy, $\langle H\rangle(\mathbf{x},t)$; the average mass fraction of solute, $\langle w\rangle(\mathbf{x},t)$; the liquid mass fraction of solute, $w^l(\mathbf{x},t)$; the superficial velocity of the liquid phase,* $\langle \mathbf{v}\rangle(\mathbf{x},t)$; and the pressure, $p(\mathbf{x},t)$. There are six unknown scalar fields and one unknown velocity field. For that purpose, three scalar average conservation equations (heat, mass, and solute) plus the average Navier–Stokes equation for the momentum equation are available. Therefore, three more scalar relationships are needed. These are the relations between $\langle H\rangle$ and (T, g_s), $\langle w\rangle$ and (w^l, g_s), and T and w^l. This last relationship is only valid in the mushy zone (*i.e.*, when $0 \le g_s \le 1$). The first relationship can be written as

$$\langle H\rangle = g_s H^s + (1 - g_s)\, H^l = c_p\, T + (1 - g_s)\, L \quad [1]$$

where c_p is the volumetric specific heat and is assumed to be constant and equal in both phases; and L is the volumetric enthalpy of dissolution, which is assumed to be equal to the enthalpy of fusion of the pure substance. Assuming that the lever rule applies at the microscopic scale of the DAS, the second relationship can be written as

$$\langle w\rangle = g_s\, w^s + (1 - g_s)\, w^l = w^l\,[1 - g_s\,(1 - k)] \quad [2]$$

The mass fraction in the solid, w^s, is given by kw^l, where k is the partition coefficient. This parameter, which is also assumed constant, is given by the phase diagram of the alloy. For the third relationship, it is further assumed that the liquidus of the phase diagram is a straight line of slope m, thus giving in the mushy zone, above the eutectic temperature,

*The superficial averaged velocity of the liquid phase $\langle \mathbf{v}\rangle = (1 - g_s)\mathbf{v}^l$, where $\mathbf{v}^l$, is the velocity of the fluid.

$$T = T_m + m w^l \quad [3]$$

where T_m is the melting point of the pure substance. When the eutectic temperature is reached, T and w^l are fixed by the phase diagram and $\langle H \rangle$ becomes a linear function of g_s.

The volumetric mass of the alloy has been assumed constant and equal in both the liquid and solid phases, except in the buoyancy term of the Navier–Stokes equation (Boussinesq approximation). Assuming linear temperature and solute dependencies, the volumetric mass, ρ, of the liquid phase can be written as

$$\rho(T, w^l) = \rho_0 \left[1 - \beta_T (T - T_0) - \beta_c (w^l - w_0)\right] \quad [4]$$

where ρ_0 is a reference volumetric mass taken at temperature T_0 and solute mass fraction w_0 and β_T and β_c are the thermal and solutal expansion coefficients, respectively.

The other parameters of the alloy such as the thermal conductivity, κ, or the viscosity of the liquid phase, μ, are also taken as constant, and the solid is assumed to be fixed in space. Under these assumptions, the average conservation equations can be written as follows.[39,40]

Mass conservation equation:

$$\text{div } \langle \mathbf{v} \rangle = \text{div } [g_l \mathbf{v}^l] = 0 \quad [5]$$

As can be seen, the superficial velocity of the liquid phase $\langle \mathbf{v} \rangle$ is equal to $g_l \mathbf{v}^l$, where $\mathbf{v}^l$ is the average interdendritic velocity of the fluid phase and $g_l = (1 - g_s)$ is the volume fraction of liquid.

Heat conservation equation:

$$\frac{\partial \langle H \rangle}{\partial t} + c_p \langle \mathbf{v} \rangle \cdot \mathbf{grad}\ T - \text{div } (\kappa\ \mathbf{grad}\ T) = 0 \quad [6]$$

Solute conservation equation:

$$\frac{\partial \langle w \rangle}{\partial t} + \langle \mathbf{v} \rangle \cdot \mathbf{grad}\ w^l = 0 \quad [7]$$

In this equation, the diffusion term has been omitted because it is negligible with respect to the transport term.

Momentum conservation equation for the liquid phase:

$$\rho_0 \frac{\partial \langle \mathbf{v} \rangle}{\partial t} + \frac{\rho_0}{g_l} \left(\langle \mathbf{v} \rangle \cdot \mathbf{grad}\right) \langle \mathbf{v} \rangle - \mu\, \Delta \langle \mathbf{v} \rangle + g_l \frac{\mu}{K} \langle \mathbf{v} \rangle = \rho_0 \left[-\beta_T (T - T_0) - \beta_c (w^l - w_0)\right] g_l \mathbf{g} - g_l\, \mathbf{grad}\ p \quad [8]$$

where K is the permeability of the mushy zone. Please note that the constant gravity term, $\rho_0 g_l \mathbf{g}$, has been omitted in this equation, since it only contributes to the metallostatic pressure p, which is therefore the static pressure. In the present case, the permeability is approximated by the well-known Carman–Kozeny relationship,[43] which is equivalent to assuming that the specific surface of the solid is equal to that of uniform spheres whose diameters are equal to the secondary DAS λ_2:

$$K = \frac{\lambda_2^2 g_l^3}{180 (1 - g_l)^2} \quad [9]$$

As can be seen, the permeability tends toward infinity in the liquid phase, thus reducing Eq. [8] to the standard Navier–Stokes equation. At an increasing volume fraction of solid, the permeability tends toward zero and the drag force of the solid dominates the other contributions appearing in Eq. [8]. In this last case, the momentum conservation equation resumes to the Darcy equation describing the flow within a porous medium:

$$\langle \mathbf{v} \rangle = -\frac{K}{\mu} \left\{ \rho_0 \left[\beta_T (T - T_0) + \beta_c (w^l - w_0)\right] \mathbf{g} + \mathbf{grad}\ p \right\} \quad [10]$$

The initial conditions are uniform temperature and mass fraction and zero velocity within the domain. The boundary conditions are no slip (*i.e.*, $\langle \mathbf{v} \rangle = 0$) and no escape of solute on all boundaries, adiabatic condition on three boundaries, and Fourier condition on the left boundary with a constant heat transfer coefficient (Table I).

IV. FINITE VOLUME FORMULATION

The control volume-based finite-difference formulation is a well-known method,[44] which is employed in many problems involving transport phenomena. In such a method, the computational domain is subdivided into control volumes, which do not overlap. All the scalar unknowns are computed at a point located at the center of each control volume, while the velocities are computed at the faces of the control volume. That means that staggered grids are employed for the discretization of the momentum Eq. [8]. The conservation Eqs. [5 through 8] are discretized by integration in space over each control volume and in time using a fully implicit formulation. The total flux (convection plus diffusion) on the faces of the control volume have been estimated using a power law scheme. A centered scheme has also been tried, except for Eq. [7], in order to investigate the effects of false diffusion. The SIMPLEC algorithm[45] has been adopted to treat the velocity-pressure coupling.

A specific algorithm is needed to deal with the nonlinearities of the equations. The basis of the numerical procedures have already been discussed in detail by Bennon and Incropera.[20] Moreover, Prakash and Voller have proposed some improvements of the method[25] for the solute conservation Eq. [7], which have been adopted in the present calculations. The main difference between our procedure and the procedures described in References 25 and 46 is in the manner in which the heat conservation Eq. [6] is discretized. Instead of considering a source term in order to obtain a discretized equation, which depends only on the average enthalpy[46] or on the temperature,[25] Eq. [6] is integrated in its natural form, *i.e.*, with two main variables: the average enthalpy and the temperature. Using the nomenclature of the finite volume formulation of Patankar,[44] the integration of Eq. [6] in time and space over a control volume can be written as

$$a_p^0 H_p^{t+\Delta t} + (a_E + a_W + a_N + a_S) T_p^{t+\Delta t} = a_E T_E^{t+\Delta t} + a_W T_W^{t+\Delta t} + a_N T_N^{t+\Delta t} + a_S T_S^{t+\Delta t} + a_p H_p \quad [11]$$

where

$$a_E = D_e A\left(|P_e|\right) + \max\left(-F_e, 0\right) \quad [12a]$$

$$a_W = D_w A\left(|P_w|\right) + \max\left(F_w, 0\right) \quad [12b]$$

$$a_N = D_n A\left(|P_n|\right) + \max\left(-F_n, 0\right) \quad [12c]$$

$$a_S = D_s A\left(|P_s|\right) + \max\left(F_s, 0\right) \quad [12d]$$

$$a_p^0 = \frac{\Delta x\, \Delta y}{\Delta t} \quad [12e]$$

The uppercase indexes P, E, W, N, and S refer to the nodal points, whereas the lowercase indexes e, w, n, and s indicate the position of the corresponding boundary faces of the volume element. $D_i = \kappa_i (S_i/\delta_{IP})$, where S_i is the surface of boundary i ($i = e$, w, n, or s) and δ_{IP} is the distance between the central point P and the neighbor I ($I = E$, W, N, or S). $F_i = c_p u_i S_i$ ($i = e$ or w) and $F_i = c_p v_i S_i$ ($i =$ n or s), where u_i and v_i are the x and y components of the velocity taken on face i, respectively. A ($|P_i|$) is a decentering function[44] of the Peclet number P_i, where $P_i = c_p \frac{u_i\, \delta_{IP}}{\kappa_i}$ ($i = e$ or w) and $P_i = c_p \frac{v_i\, \delta_{IP}}{\kappa_i}$ ($i = n$ or s).

The average enthalpy has been chosen as the principal variable in Eq. [11], since dT/dH can be quite small during phase transformation (it can even be zero during isothermal transformation). In a first step, the temperature is linearized using Newton's method:

$$T^{t+\Delta t} = T^n + \left(\frac{dT}{dH}\right)^{(n)} \left[H^{t+\Delta t} - H^{(n)}\right] \quad [13a]$$

$$T^{(n=0)} = T^t,\ H^{(n=0)} = H^t \quad [13b]$$

where n is the iteration index. Replacing the unknown temperature of Eq. [11] by the expression [13a] leaves the enthalpy as the only unknown. The time derivative, $(dT/dH)^{(n)}$, is calculated as follows:

$$\text{if } g_l = 1 \qquad \frac{dT}{dH} = \frac{1}{c_p} \quad [14a]$$

$$\text{if } 0 < g_l < 1 \text{ and } T \neq T_{\text{eutectic}} \qquad \frac{dT}{dH} = \frac{1}{c_p + L\dfrac{dg_l}{dT}} \quad [14b]$$

$$\text{if } 0 < g_l < 1 \text{ and } T = T_{\text{eutectic}} \qquad \frac{dT}{dH} = \frac{1}{10c_p} \quad [14c]$$

$$\text{if } g_l = 0 \qquad \frac{dT}{dH} = \frac{1}{c_p} \quad [14d]$$

Please note that an arbitrarily small value of dT/dH is taken on the eutectic plateau instead of 0; otherwise, this would make the scheme locally explicit. It is interesting to note that the estimation of dT/dH in Eq. [13a] is not very important, because the last term on the right side of Eq. [13a] vanishes when convergence is reached.

Details relative to this method have already been presented by the authors in connection with simulations of the formation of macrosegregation in heavy steel ingots.[26] A similar method has also been used earlier by Desbiolles *et al.*[46] for micro-macromodeling of solidification.

Since all transfers are coupled, an iterative solving procedure is used, as follows:

(1) compute $\langle H \rangle$ from Eq. [6];
(2) compute $\langle w \rangle$ from Eq. [7];
(3) compute $\langle v \rangle$ from Eq. [8];
(4) compute p from Eq. [5] and correct the velocity field in order to verify the global mass conservation; and
(5) compute T, w^l, and g_l from Eqs. [1] through [3] by a procedure similar to that proposed in Reference 47.

This sequence of operations is repeated until convergence is achieved before advancing to the next time-step. The benchmark problem of De Vahl Davis and Jones[48] has been used to validate the program.

Computations have also been performed without iterations inside a time-step in order to investigate the sensitivity of the results to an iterative procedure

V. FINITE ELEMENT FORMULATION

The evolutive average conservation equations given in Section III have been solved using a fully implicit time-stepping scheme and a standard Petrov–Galerkin formulation.[49] The details of this formulation can be found in Reference 42, and only the key points are given here.

The rectangular domain has been enmeshed with quadrangle elements, with bilinear functions for all the fields except the pressure field, which is assumed to be constant within each element (*i.e.*, Q_1-P_0 element for the velocity-pressure fields). This means that any field, $\phi(\mathbf{x},t)$, except the pressure, is written as an expansion:

$$\phi(\mathbf{x},t) = \sum_i \phi_i(t)\, \psi_i(\mathbf{x}) \quad [15]$$

The summation is made over all the nodal points of the enmeshment, the $\psi_i(\mathbf{x})$ being the bilinear function associated with node (i). Since all the equations, except that of mass conservation, are of mixed convection-diffusion type, an upwinding scheme has been used.[49,50] This means that the test functions used in the weak FEM formulation are given by

$$\tilde{\psi}_j(\mathbf{x}) = \psi_j(\mathbf{x}) + \theta \frac{\langle \mathbf{v} \rangle \cdot \mathbf{grad}\ \psi_j}{\|\langle \mathbf{v} \rangle\|} h \quad [16]$$

where θ is an upwind parameter[49] and h is a typical size of the element. In this way, the first derivative of any field ϕ is shifted along the streamlines in the upwind direction by an amount θ. With $\theta = 0$, there is no upwinding and the FEM scheme resumes to a standard formulation. The parameter θ can be optimized as a function of the Péclet number of the mesh,[49] but it is sufficient in most cases to make a "full" upwinding for which $\theta = 1/2$. In the remainder of the article, this scheme will be referred to as the streamline upwind Petrov–Galerkin (SUPG) formulation.[49]

The three average conservation equations of heat, momentum, and solute are solved separately at each time-step in this sequence, similarly to what has been presented in Section IV. More specifically, the solution scheme is as follows.

(1) The equation of heat is formulated according to an enthalpy scheme, using only one Newton's step (Eq. [13a] with $n = 0$).

(2) The momentum conservation equation is solved using the most recent temperature and solute fields appearing in the buoyancy term (Eq. [4]). Similarly, the most recent volume fraction of liquid (or solid) field is used in this equation. The nonlinear Stokes term of Eq. [8] is linearized according to $(\langle \mathbf{v} \rangle^t \cdot \mathbf{grad})\, \langle \mathbf{v} \rangle^{t+\Delta t}$. The pressure term appearing in this equation is eliminated using a penalty method.[50] For that purpose, the incompressibility condition (Eq. [5]) is replaced by

$$\text{div}\, \langle \mathbf{v} \rangle = -\varepsilon_p\, p \qquad [17]$$

where ε_p is an arbitrarily small value (typically 10^{-10}). The insertion of Eq. [17] into Eq. [8] gives

$$\rho_0 \frac{\langle \mathbf{v} \rangle^{t+\Delta t} - \langle \mathbf{v} \rangle^t}{\Delta t} + \frac{\rho_0}{g_l} \left(\langle \mathbf{v} \rangle^t \cdot \text{grad} \right) \langle \mathbf{v} \rangle^{t+\Delta t} - \mu \Delta \langle \mathbf{v} \rangle^{t+\Delta t} + g_l \frac{\mu}{K} \langle \mathbf{v} \rangle^{t+\Delta t} - \frac{g_l}{\varepsilon_p} \text{grad div} \langle \mathbf{v} \rangle^{t+\Delta t} = \rho_0 \left[-\beta_T (T - T_0) - \beta_c (w^l - w_0) \right] g_l\, \mathbf{g} \qquad [18]$$

Taking all the other fields (*e.g.*, T, w^l, g_l, . . .) as the most recently calculated ones, Eq. [18] gives the new velocity field $\langle \mathbf{v} \rangle^{t+\Delta t}$ at the nodal points.

(3) Using the new velocity field, the variation of average mass fraction, $\Delta \langle w \rangle$, at each nodal point is calculated according to Eq. [7]. For that purpose, a diffusion term is first introduced in this equation, which becomes

$$\frac{\partial \langle w \rangle}{\partial t} + \langle \mathbf{v} \rangle \cdot \mathbf{grad}\, w^l - \text{div} (\varepsilon\, \mathbf{grad}\, w^l) = 0 \qquad [19]$$

In this equation, the diffusion term is negligible with respect to the transport term especially for the solid phase, and accordingly, only w^l appears in this term. The diffusion coefficient ε could be written as $g_l D^l$ if diffusion in the liquid phase only is considered, but any arbitrarily small value is convenient and does not influence the results. The diffusion term has been kept in Eq. [19] mainly for numerical reasons: it is easier to make a formulation of a diffusion-convection equation rather than a purely transport equation.

Following a procedure similar to that of Voller,[25] this equation is formulated as follows:

$$\frac{\langle w \rangle^{t+\Delta t} - \langle w \rangle^t}{\Delta t} + \langle \mathbf{v} \rangle \cdot \mathbf{grad}\, \langle w \rangle^{t+\Delta t} - \text{div} (\varepsilon\, \mathbf{grad}\, \langle w \rangle^{t+\Delta t}) = \langle \mathbf{v} \rangle \cdot \mathbf{grad} \left(\langle w \rangle^t - w^{l,t} \right) - \text{div} \left(\varepsilon\, \mathbf{grad} \left(\langle w \rangle^t - w^{l,t} \right) \right) \qquad [20]$$

As can be seen, "split operators" have been used in this case in order to obtain an implicit scheme: the mass fraction w^l appearing in Eq. [7], which, in an implicit scheme, should be taken at the next time-step, has been replaced by $w^{l,t+\Delta t} \cong w^{l,t} + \langle w \rangle^{t+\Delta t} - \langle w \rangle^t$.

In summary, the three equations governing heat, solute, and momentum are solved at each time-step, thus giving the new average enthalpy, $\langle H \rangle^{t+\Delta t}$, velocity, $\langle \mathbf{v} \rangle^{t+\Delta t}$, and mass fraction, $\langle w \rangle^{t+\Delta t}$, at each nodal point. The new temperature, $T^{t+\Delta t}$, mass fraction in the liquid, $w^{l,t+\Delta t}$, and volume fraction of solid, $g_s^{t+\Delta t}$, are then updated according to the phase diagram. A procedure similar to that described in Reference 47 is used, assuming local equilibrium (*i.e.*, lever rule).

It can be noticed that the scheme of resolution of Eqs. [5] through [8] presented in this section is similar to that presented in the FVM, where iterations are not performed inside a time-step.

VI. RESULTS AND DISCUSSION: A COMPARISON BETWEEN FEM AND FVM PREDICTIONS

Figure 2 shows the streamlines within the liquid and mushy zones and the maps of the volume fraction of solid, as calculated for the Pb-48 wt pct Sn alloy using FVM (left) and FEM (right), after 50 seconds of cooling. The streamlines are defined as the isovalues of the hydrodynamic stream function ψ, where ψ is such that $v_x = (\partial \psi / \partial y)$ and $v_y = -(\partial \psi / \partial x)$. As can be seen, the trends predicted by both schemes are the same: the flow is essentially cw and ψ increases from the center to the periphery of the vortex. Since the streamline function ψ is defined with an unspecified integration constant, only the streamline increment separating the isolines, $\Delta \psi$, has been mentioned in the figure caption for both schemes, together with the maximum velocity, v_{max}, calculated at that time. As can be seen, the agreement between the two predictions of the streamlines is quite good: the centers of the vortex and the overall shape of the streamlines correspond fairly well. Clearly, convection in this case is dominated by solutal convection, and the rejected tin atoms have a tendency to make the interdendritic fluid lighter; therefore, it flows upward (*i.e.*, cw vortex). The predictions supplied by the two softwares are very close to each other in the mushy zone, where the driving force of the liquid flow is located. However, morphological differences are much more pronounced in the full liquid area. This can be seen clearly in the right part of the cavity and near the top boundary. Furthermore, the maximum velocity predicted by FEM is slightly higher than that obtained by FVM. Several possible explanations of such differences have been investigated, after a careful check of the equations and parameter values.

In the FVM scheme, iterations are performed at each time-step, which is not the case for FEM. A test calculation was performed without iterations in the FVM scheme. The main difference observed with or without iterations appeared in the fluid flow field, the agreement between the FVM and FEM predictions being better in the absence of iterations. The maximum velocity predicted with FVM is slightly increased (14 pct) but still remains lower than that predicted by FEM. On the other hand, the maps of segregation, volume fraction of solid, and temperature field remain nearly unchanged when no iteration is made. A refinement of the grid did not change appreciably the results, and thus, the different interpolation methods used in both schemes could hardly be incriminated. It must also be kept in mind that, for the two alloys, the Prandtl number, which estimates the ratio of the momentum diffusivity to the thermal diffusivity (*i.e.*, $\text{Pr} = (\nu/\alpha)$, where $\alpha = (\kappa/c_p)$ and $\nu = (\mu/\rho)$) is of the order of 10^{-3}. For such low Prandtl numbers, it has been shown that oscillatory phenomena may occur in the case of thermal natural convection, which

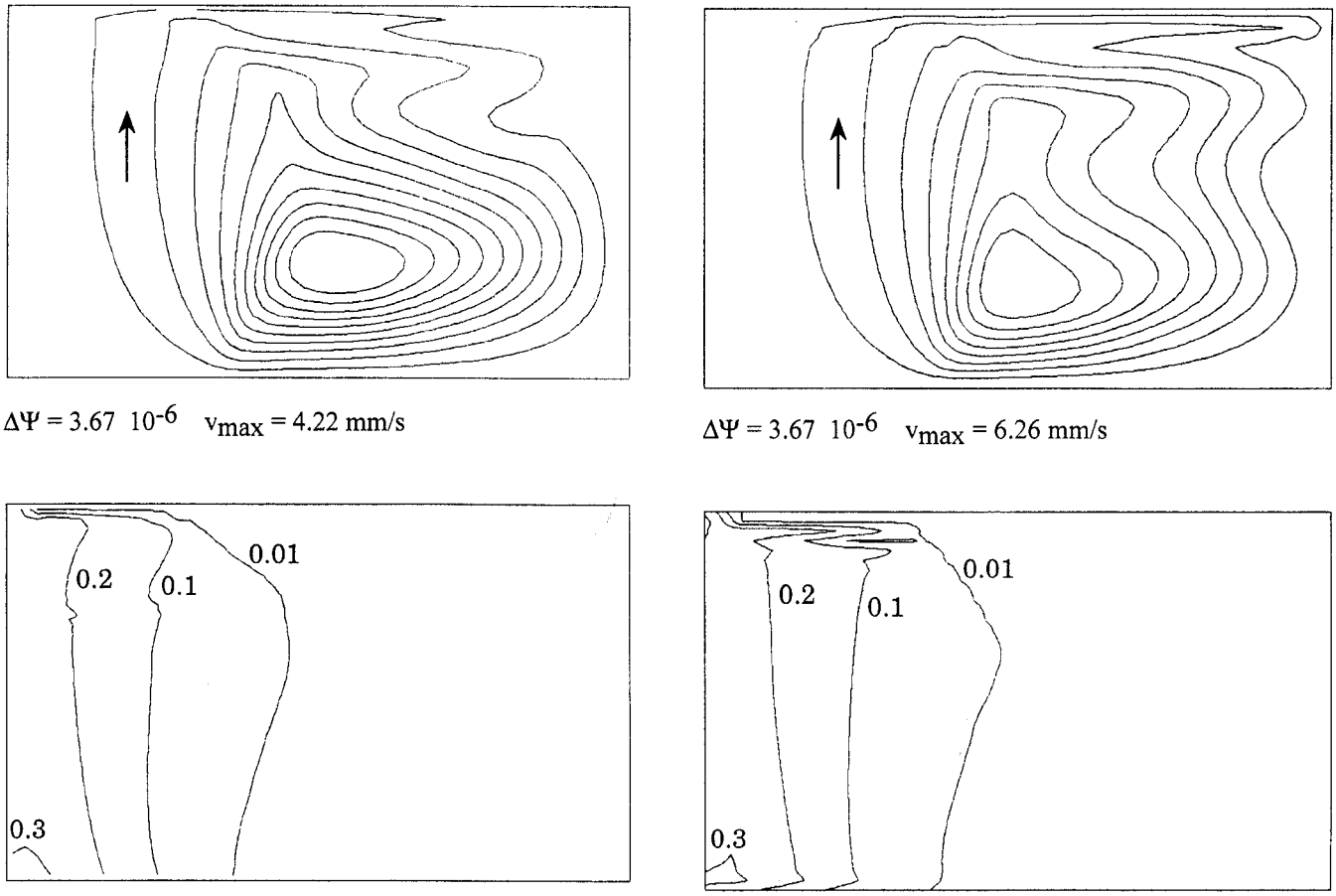

Fig. 2—Numerical results of the FVM (left) and FEM (right) segregation calculations obtained with the Pb-48 wt pct Sn alloy: streamlines (top) and volume fraction of solid (bottom) after 50 s.

Table I. Thermophysical Data and Parameters Used in the Calculations

		Pb-48 Wt Pct Sn	Sn-5 Wt Pct Pb
Phase diagram data			
Initial mass fraction	wt pct	48.0	5.0
Melting temperature	°C	327.5	232.0
Eutectic temperature	°C	183.0	183.0
Liquidus slope	°C wt pct^{-1}	−2.334	−1.286
Distribution coefficient	—	0.307	0.0656
Eutectic mass fraction	wt pct	61.9	38.1
Thermal data			
Specific heat (liquid or solid)	J kg^{-1} °C^{-1}	200.0	260.0
Thermal conductivity (liquid or solid)	W m^{-1} °C^{-1}	50.0	55.0
Latent heat of fusion	J kg^{-1}	53,550	61,000
Other characteristics			
Reference volumetric mass	kg m^{-3}	9000	7000
Reference temperature	°C	232	226
Thermal expansion coefficient	°C^{-1}	$1 \cdot 10^{-4}$	$6 \cdot 10^{-5}$
Solutal expansion coefficient	wt pct^{-1}	$4.5 \cdot 10^{-3}$	$-5.3 \cdot 10^{-4}$
Dynamic viscosity	kg m^{-1} s^{-1}	$1 \cdot 10^{-3}$	$1 \cdot 10^{-3}$
Secondary dendrite arm spacing	μm	40	65
Calculation parameters			
Initial temperature	°C	216	226
Time-step	s	0.1	0.05
Heat transfer coefficient	W m^{-2} °C^{-1}	400	300
External temperature (T_0)	°C	25	25
Number of nodes in X direction	—	50	60
Number of nodes in Y direction	—	40	60

cannot be captured by a first-order scheme. Thus, the schemes used in the present FVM and FEM formulations may not be accurate enough to describe the fluid motion in the present cases.

The upwind procedure, which is not made along the streamlines in the FVM scheme unlike the FEM one, could have some influence on the results since it adds some numerical diffusion/viscosity. With velocities of the order of mm/s, this cause was also eliminated by using various upwinding schemes in FVM (central difference scheme, full and controlled upwinding), as will be shown near the end of this section. The explanation that is most likely to explain the small discrepancies observed in Figure 2 might be due to the boundary conditions. In FEM, the velocities are imposed directly on the edges of the cavity and are set to zero in the case of no slip. However, in FVM, the no-slip condition is expressed by using a condition on the tangential stress component, since the first horizontal velocities are displaced inward by half a mesh size of the staggered grid. It has been observed that the boundary layer at the upper edge of the cavity is very thin and that a finer mesh might be needed in the case of FEM since the maximum velocity occurs at the first nodal point.

Another explanation could be found in the discretization of the friction term $g_l(\mu/K)\langle \mathbf{v} \rangle$ in Eq. [8]. With the FEM scheme, permeability is calculated at the Gauss points of the elements and the velocity is taken without upwinding correction. In the FVM formulation, the values of the permeability are known at the center of each cell, where the scalar quantities are calculated, whereas the velocity components are computed on the four edges. The calculation of the permeability K_i at the position of face i is made according to $K_i^{-1} = 1/2(K_I^{-1} + K_P^{-1})$. As the permeability strongly depends on the fraction of liquid, in particular, when g_l is close to zero, the asymptotic behavior of the friction term combined with the different discretization methods may lead to fairly large discrepancies between the two calculated velocity fields.

The maps of volume fraction of solid shown at the bottom of Figure 2 are also in good agreement: their shapes and positions correspond fairly well, although the $g_s = 0.01$ isoline delimiting the dendrite tip position is slightly more edgy in the case of FEM. The effects of the different techniques used to model the no-slip boundary conditions can be clearly observed at the bottom boundary; the isolines predicted by FEM have a small cusp at this boundary, whereas those obtained by FVM are drawn only up to a half-mesh size and are smooth. The small cusp disappears when slip is allowed on the boundaries. This difference is another argument in favor of the explanation given before for the streamlines. At the top of the cavity, a layer of tin-rich liquid accumulates as a result of the cw convection, and thus, the isofractions of solid are nearly horizontal. A small tendency toward segregated channels is seen in the FEM results near this boundary (*i.e.*, oscillations of the values of g_s along a vertical line). This is due to the fact that close to the top of the cavity, the interdendritic liquid has a velocity nearly parallel to the speed of the isotherms. Such a tendency to form segregated channels is less pronounced in the FVM results. A small bump can be seen, however, in the isolines $g_s = 0.1$ and 0.2.

Figure 3 presents for the same alloy the isotherms (top) and the segregation isopleths (bottom) after 400 seconds of cooling. The FVM results are again shown on the left, whereas those obtained with FEM are on the right. A very good agreement is noticed, especially for the isotherms. The isotherms are bent in the cw direction as a result of the fluid flow; surprisingly, it is slightly less bent in the FEM results, while the maximum velocity was higher at $t = 50$ seconds (Figure 2). This might be due to the shape of the streamlines, which are more vertical in the right part of the cavity (Figure 2). A small bump is observed in the FVM isotherm $T = 183$ °C; it corresponds to the eutectic temperature at which g_s is not a continuous function. The maps shown at the bottom of Figure 3 indicate the relative variation of tin mass fraction (*i.e.*, $\Delta\langle w \rangle / w_0 = (\langle w \rangle - w_0)/w_0$, where w_0 is the nominal mass fraction). The neutral line (0 pct) extends from the upper left to the bottom right corner of the cavity and has nearly the same position and shape in both the FVM and FEM results. The region below this line is characterized by a negative macrosegregation, slightly more pronounced in the FVM results, whereas the upper right zone has a positive segregation index, again more pronounced in FVM. The upper left region of the ingot is characterized by a high gradient of tin mass fraction in the two formulations. The tin mass fraction goes from zero to the maximum positive value over one or two cells. The FVM results show a segregated channel of very low intensity (between −2 and 0 pct) whose location corresponds to the bump already observed on the isofractions of solid (Figure 2). This channel is inclined with respect to the ingot boundaries and looks like those calculated numerically by Schneider and Beckermann[14] (using an isotropic permeability function and similar boundary conditions) or the A segregates shown experimentally by Fredriksson and Nilsson on a Pb-5 wt pct Sn alloy.[51] Such a channel can also be seen in the results of Prescott and Incropera for a Pb-19 wt pct Sn alloy in an axisymmetric situation cooled from the lateral side.[19] On the other hand, the isolines of mass fraction predicted by FEM in the same upper-left area show a set of confined horizontal channels of fairly high intensity (between 0 and 15 pct). A possible explanation of these discrepancies will be proposed in Section VII.

Before comparing the final segregation maps predicted by FVM/FEM with the experimental results of HH, calculated streamlines, isofractions of solid, isotherms, and isolines of mass fraction are presented for the Sn-5 wt pct Pb alloy in Figures 4 and 5. The streamlines and isofractions of solid are shown after 100 seconds of cooling in Figure 4 (FVM results on the left, FEM ones on the right). In this case, the flow is ccw as a result of lead rejection in between the tin dendrite arms. Therefore, the streamline values decrease from the center of the vortices to the periphery. The maximum velocity calculated with the two numerical techniques is indicated in the figure caption together with the streamline value increment. Again, the agreement between the FVM and FEM results is very good despite the slightly larger value of v_{max} calculated in this case with the FVM technique. Two ccw vortices with a stagnant region in between are seen in both results, their centers and shapes being very similar. The positions of the isofraction of solid lines are also in very good agreement. Both schemes predict an accumulation of lead mass fraction and the formation of

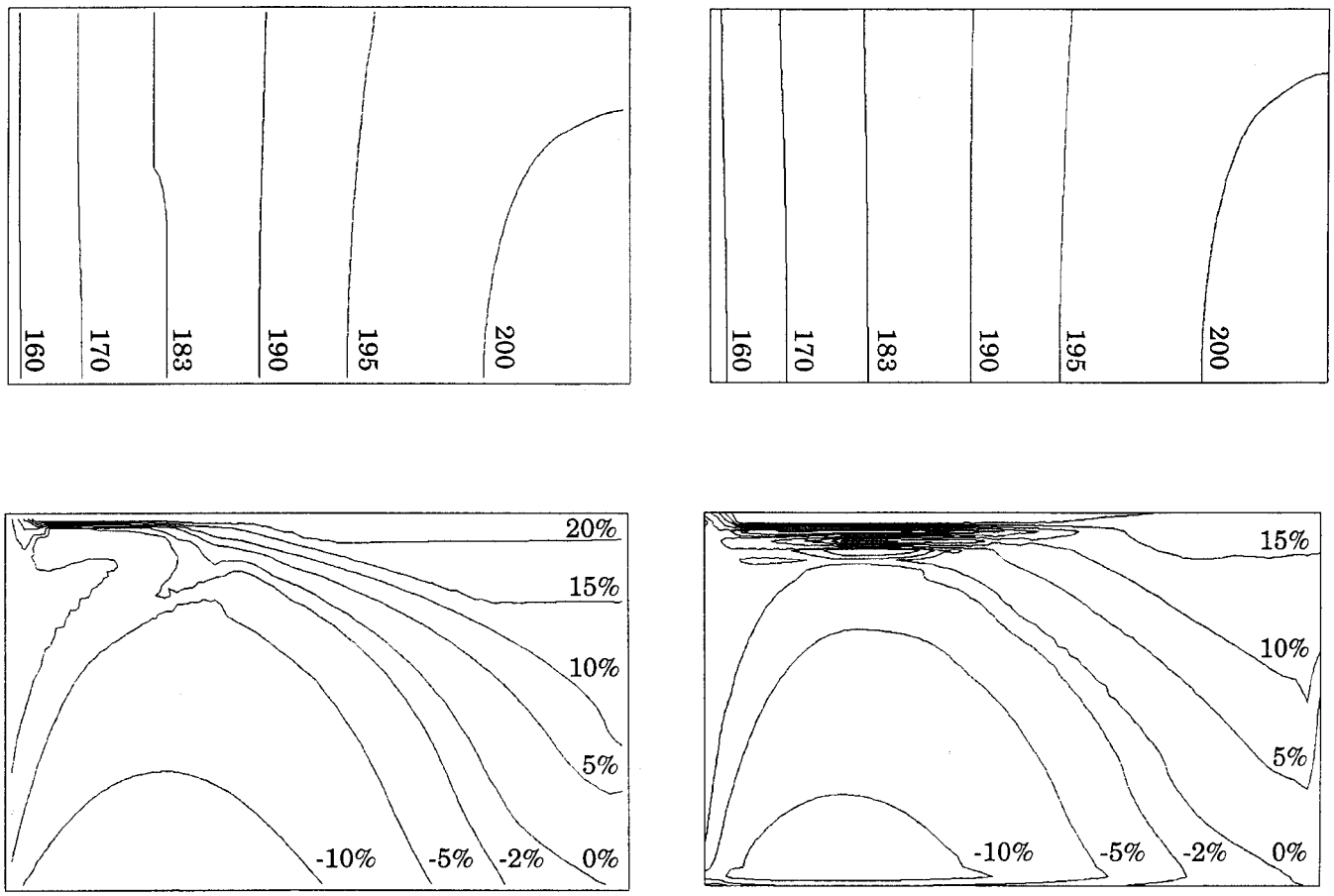

Fig. 3—Numerical results of the FVM (left) and FEM (right) segregation calculations obtained with the Pb-48 wt pct Sn alloy: thermal field (top) and relative tin mass fraction variation (bottom) after 400 s.

a liquid layer at the bottom boundary. It can be noticed that the tendency toward segregated channel formation is now inverse: the FVM simulation predicts some oscillations near the bottom of the boundary, particularly visible on the line $g_s = 0.1$. This trend is much less pronounced in the FEM results even though a small instability is seen in this region.

The temperature maps shown at the top of Figure 5 for the tin-lead alloy after 400 seconds of cooling are also in good agreement: as a result of the ccw convection, the isotherms are bent in this direction. The deflection of the 225°C isotherm with respect to the vertical direction is more pronounced for the FEM result. This is due to the slightly larger velocities predicted with this scheme in the lower part of the cavity. Concerning the relative segregation maps shown at the bottom of Figure 5, the agreement between the FVM and FEM predictions is very good near the top and on the right side of the cavity. Both formulations predict a segregated channel confined at the bottom of the cavity and extending over nearly the entire length of the ingot. As for the lead-tin alloy, the differences between the FVM and FEM results are again observed for the segregated channels, which develop in the inner part of the ingot. The FVM results show a set of segregated channels of very low intensity (between 0 and 5 pct), which are diffusing deep inside the ingot. As in Figure 3, these channels extend from the inner part of the cavity to the boundaries and are similar to those found experimentally by Fredriksson and Nilsson[51] for an alloy of nearly the same composition (Sn-10 wt pct Pb). Their locations correspond to the flow instabilities that can be seen on the streamlines of Figure 4. On the other hand, the FEM results exhibit higher intensity horizontal channels, which are confined in a small region just above the large bottom remelted channel. Schneider and Beckermann[14] already pointed out that the permeability model used for the description of the mushy zone strongly influences the orientation and number of segregated channels. Therefore, the numerical formulation of the permeability term, which is slightly different in the two codes, might be the cause of the discrepancies seen in Figure 5.

In order to study the influence of the numerical scheme, and in particular of the upwinding procedure, a few calculations have been made with different viscosities. The result of such a computation is shown in Figure 6. The maximum velocity, v_{max}, observed in the HH cavity 10 seconds after the beginning of cooling is plotted as a function of the value of the viscosity for the Pb-48 wt pct Sn alloy. The three curves plotted in Figure 6 correspond to the FEM results with the SUPG scheme (continuous line and circles), the FVM results with a centered scheme (dashed line and triangles), and the FVM results with a controlled upwinding or power law scheme (dotted lines with squares). The value used in the previous calculations for comparison with the HH results is indicated in the figure ($\mu = 1 \cdot 10^{-3}$ Pa s).

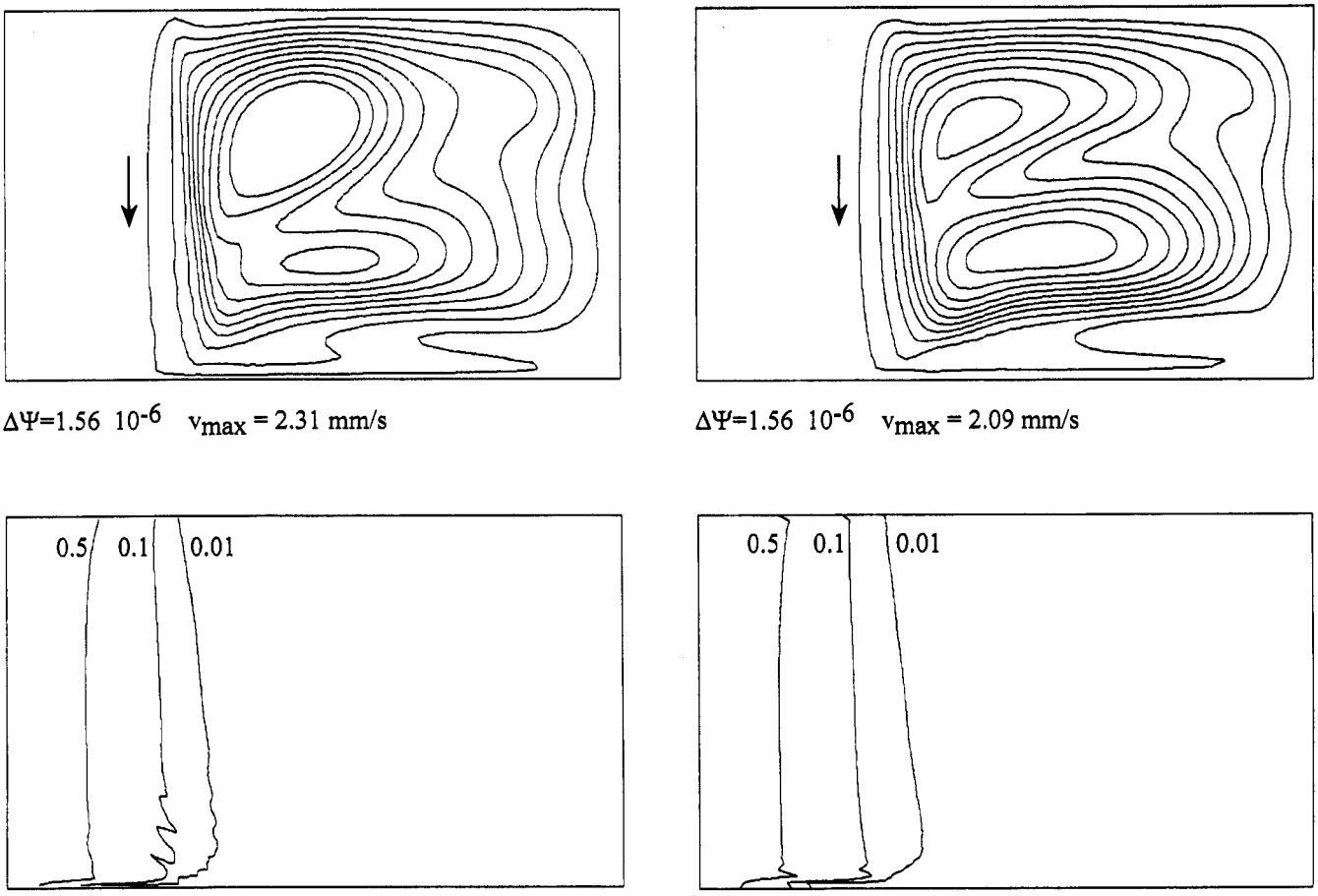

Fig. 4—Numerical results of the FVM (left) and FEM (right) segregation calculations obtained with the Sn-5 wt pct Pb alloy: streamlines (top) and volume fraction of solid (bottom) after 100 s.

As can be seen, the numerical scheme has a minor effect with this value of μ. A decrease of the viscosity increases the maximum velocity, and thus the macrosegregation. However, with decreasing values of μ, the influence of the numerical viscosity becomes more important as well. At $\mu = 10^{-6}$ Pa s, the most diffusive scheme is the FVM technique with a power law upwinding. Indeed, the upwinding is not made along the streamlines in this case and numerical diffusion occurs both along and perpendicularly to the streamlines. With the FEM scheme, the upwinding is made along the streamlines and the numerical diffusion is better controlled. The FVM scheme with no upwinding produces the highest v_{max} and thus is the least diffusing. However, no upwinding might create wiggles near downwind boundaries where an imposed value (Dirichlet condition) is fixed.

Finally, it is of some interest to compare the computing times associated with both codes. All the calculations have been carried out on an HP* 9000S735 computer. With the parameters given in Table I for the Pb-48 wt pct Sn alloy, the FVM calculation took 4.8 hours with iterations in a time-step and 0.8 hours without. For the Sn-5 wt pct Pb case, it took 31 and 18 hours with and without iterations, respectively. The FEM calculations took 8.5 hours for the Pb-48 wt pct Sn case and 53.3 hours for the Sn-5 wt pct Pb. For the two numerical methods, the difference of CPU times between the two cases reflects the larger number of nodal points (3600 compared with 2000) and the smaller time-step (0.05 seconds compared to 0.1 seconds) used for the tin-lead alloy. It can be noticed first that an iterative procedure is very time consuming while not bringing clearly different results. The ratio between the CPU times with and without iterations is not a constant and may be very large (one order of magnitude for the Sn-5 wt pct Pb case). Without iterations in a time-step, the FVM computation time is much smaller that the FEM one, but this advantage will be counterbalanced by the increased number of nodal points needed to represent a domain of complex geometry.

*HP is a trademark of Hewlett-Packard Company, Colorado Springs, CO.

VII. RESULTS AND DISCUSSION: CONFRONTATION OF NUMERICAL PREDICTIONS WITH EXPERIMENTS

The goal of this contribution was, first, to compare together the results of the FVM and FEM formulations and, second, to see how they could match the experimental results of HH. The final segregation maps obtained after complete solidification are compared in Figures 7 and 8 for the Pb-48 wt pct Sn and Sn-5 wt pct Pb alloys, respectively. In these figures, the relative variations of the average mass

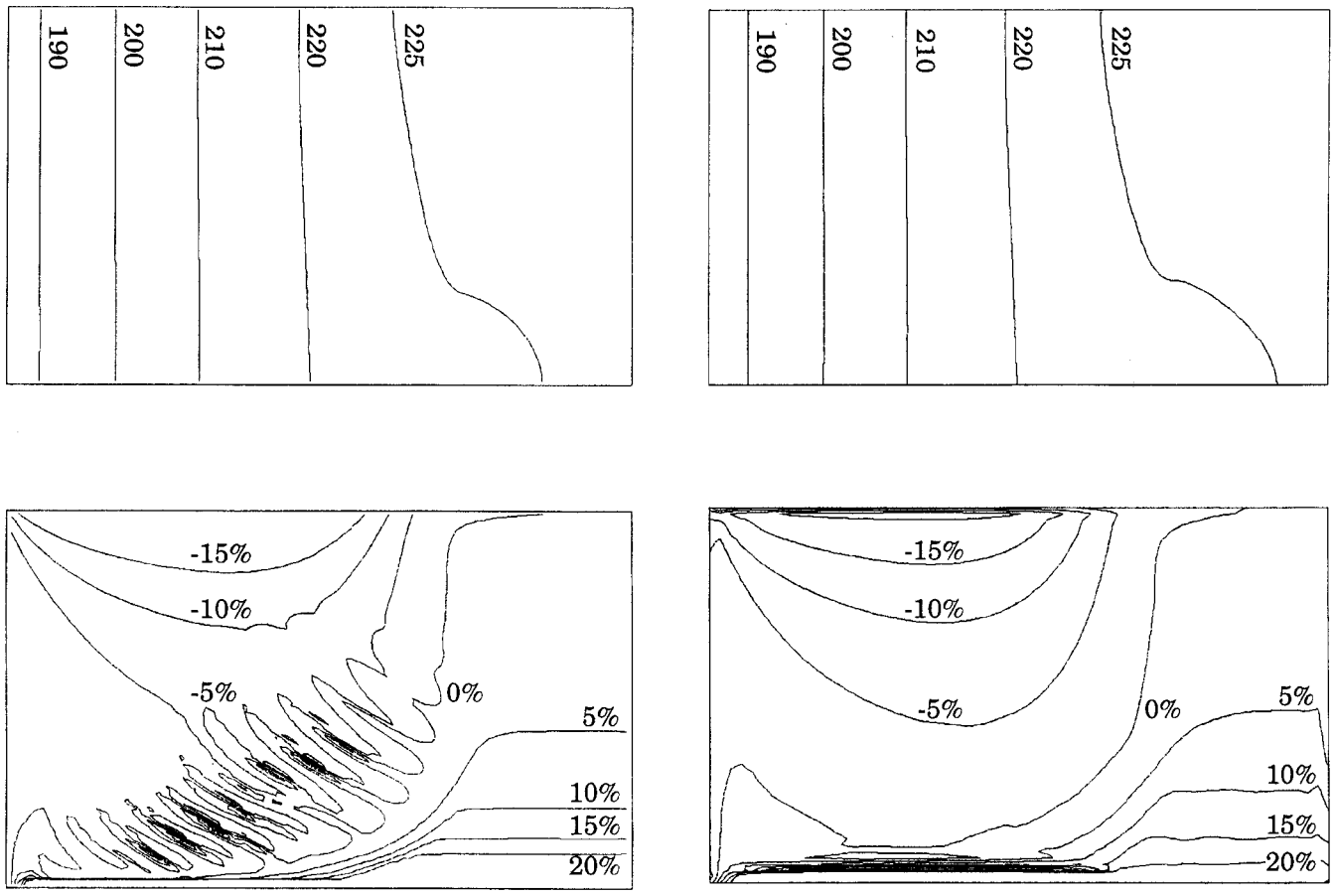

Fig. 5—Numerical results of the FVM (left) and FEM (right) segregation calculations obtained with the Sn-5 wt pct Pb alloy: thermal field (top) and relative lead mass fraction variation (bottom) after 400 s.

fraction, $\Delta\langle w\rangle/w_0$ (tin or lead), are plotted as a function of the distance to the chill for four heights: 0.5, 2.5, 3.5, and 5.5 cm from the bottom boundary. On each figure, the results of the FVM (continuous line) and FEM (dashed line) calculations are compared with the HH results (open circles). In the case of the Pb-48 wt pct Sn alloy (Figure 7), the results are in excellent agreement for the first three heights. Near the top of the cavity, where tin accumulates, the trend to positive segregation is well reproduced by both models, but the agreement is not as good. This might come from the freckling tendency, which was not mentioned in the HH article, and possibly from the shrinkage, which was not accounted for in the simulation. Shrinkage is known to be responsible for inverse segregation,[13] but it also displaces downward the final surface of solidification. Therefore, we are not sure that the simulation and experimental results are compared at the same height in a region where the tin mass fraction varies quite dramatically. Similar observations can be made for the Sn-5 wt pct Pb alloy (Figure 8). The agreement is good in the upper part of the cavity (5.5 cm), where solidification starts first (negative segregation). The agreement is less satisfactory near the bottom of the cavity (0.5 cm), where a strong positive segregation is observed at the end of solidification (more than 100 pct at the bottom right corner). It seems that the FVM results match slightly better the experimental results in this region. The tendency to freckling appears as small oscillations in the FVM mass fraction profiles.

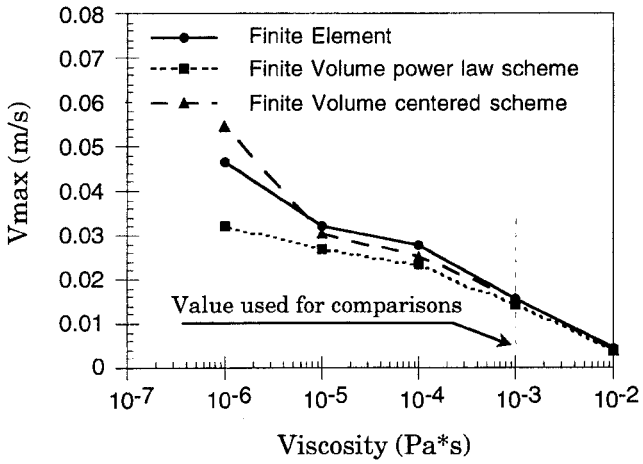

Fig. 6—Study of the influence of the numerical scheme and viscosity on the maximum velocity in the cavity 10 s after the beginning of cooling. FEM results are obtained with a SUPG method and FVM with a power law and a centered scheme.

The list of parameters that can influence the segregation results presented in Figures 2 through 8 is quite long (Table I). The parameters entering the model have been either taken from experimental findings (*e.g.*, phase diagram data) or fitted to the segregation results. They were the same for the FVM and FEM simulations, although better agreement could have been found with the experimental results if

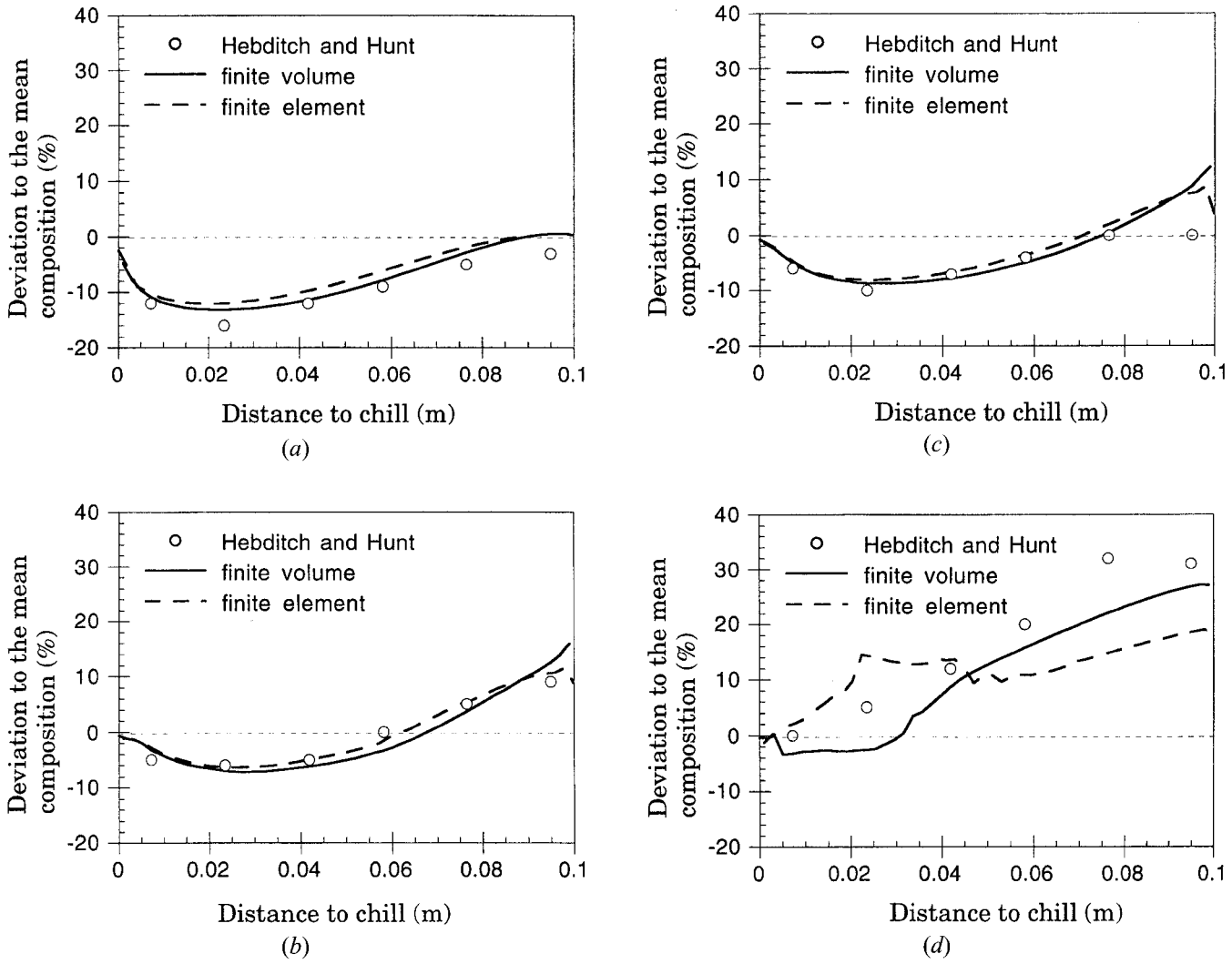

Fig. 7—Relative tin mass fraction variations for the Pb-48 wt pct Sn alloy at the end of solidification as a function of the distance to the cold surface. The continuous/dashed curves calculated with FVM/FEM are compared with the measurements of HH (open circles). These profiles correspond to various heights from the bottom of the cavity: (*a*) 0.5 cm, (*b*) 2.5 cm, (*c*) 3.5 cm, and (*d*) 5.5 cm.

slightly different parameters had been selected for a particular numerical technique. Therefore, it was quite natural to make a sensitivity analysis in order to assess the influence of each of these parameters. Among these, it appeared that the viscosity of the liquid and the permeability of the mushy zone influenced most sensitively the segregation results. This latter parameter was varied *via* a change of the DAS but taken as constant and uniform in each calculation. The summary of this sensitivity analysis is shown in Figure 9 for the Pb-48 wt pct Sn alloy. In this figure, the mass fraction profile at midheight of the cavity is plotted as a function of the distance to the chill side. Three values of the DAS (20, 40, and 60 μm) and of the viscosity ($0.5 \cdot 10^{-3}$, $1.0 \cdot 10^{-3}$, and $2.0 \cdot 10^{-3}$ Pa s) have been selected, and the results are shown for the FVM (left) and FEM (right) simulations. As can be seen, an increase in the DAS also increases macrosegregation, since the mush becomes more permeable to the fluid. It must be pointed out that a doubling of the DAS multiplies by a factor of 4 the permeability (Eq. [9]). It is well known that the final DAS is proportional to the 1/3-power of the local solidification time.[52] The computed times of solidification lead to a doubling of the DAS value from one part of the cavity to another. Furthermore, the DAS evolves also at any given point as a function of time. Nevertheless, it has been kept constant and uniform to make the benchmark between the two codes simpler. The influence of the boundary condition set on the right boundary of the cavity can be clearly seen in Figure 9. A decrease of the viscosity (Figure 9, bottom) also increases the final macrosegregation.

VIII. CONCLUSIONS

As a summary, it can be said that for the first time, a benchmark test has been made for macrosegregation calculations in two dimensions. Two formulations of the same average conservation equations have been used, one based upon a finite volume technique and the other upon a finite element formulation. Although the equations are strictly the same, the handling of the boundary conditions, the upwinding of the entities, the interpolation functions, and other numerical techniques such as the handling of the pressure or the iteration scheme are different. The two numerical techniques have been compared on two test cases, a rectangular cavity containing either a Pb-48 wt pct Sn or a

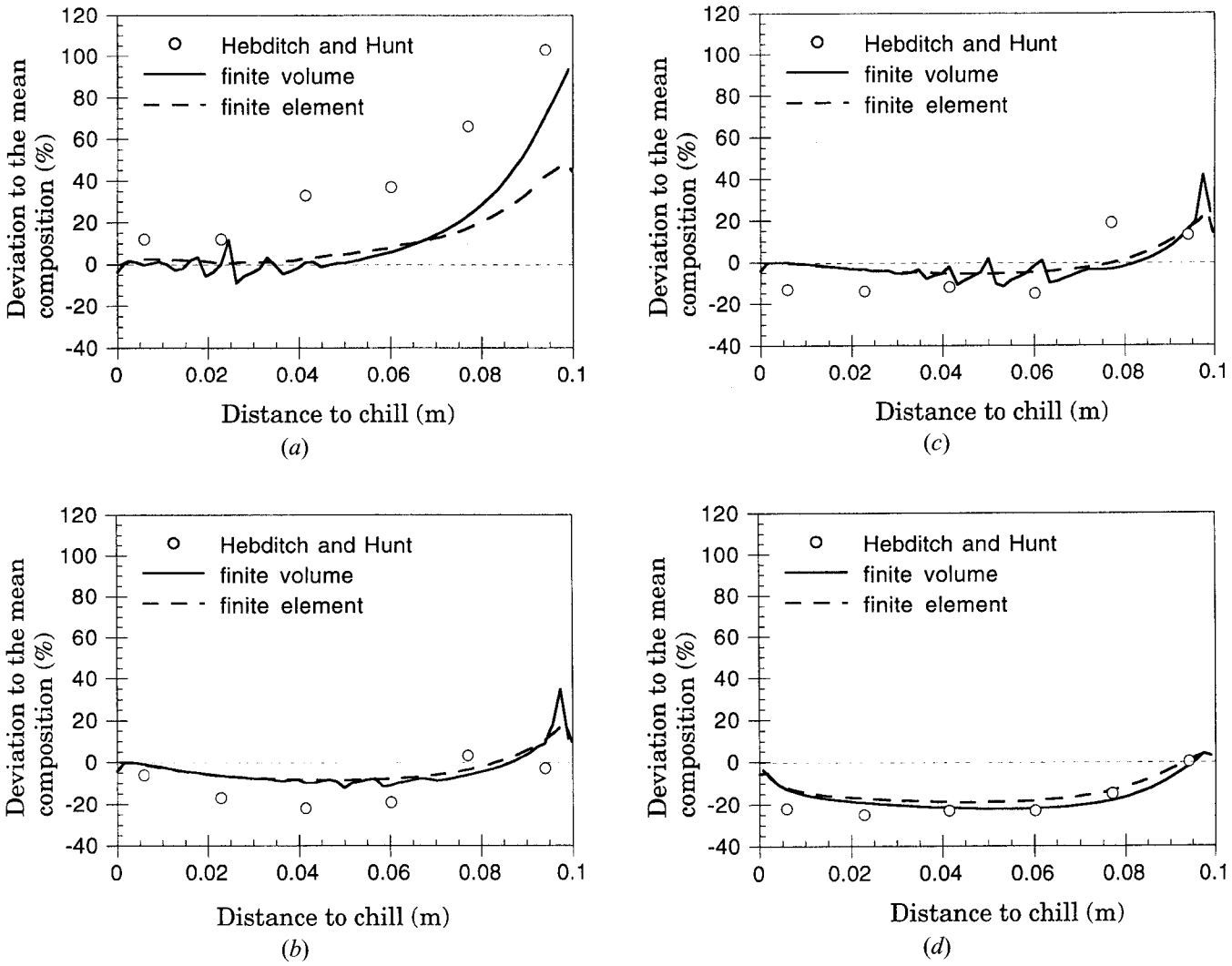

Fig. 8—Relative lead mass fraction variations for the Sn-5 wt pct Pb alloy at the end of solidification as a function of the distance to the cold surface. The continuous/dashed curves calculated with FVM/FEM are compared with the measurements of HH (open circles). These profiles correspond to various heights of the cavity: (*a*) 0.5 cm, (*b*) 2.5 cm, (*c*) 3.5 cm, and (*d*) 5.5 cm.

Sn-5 wt pct Pb alloy. In the first case, the thermal and solutal natural convections are opposite, but the latter one clearly dominates and the flow is cw. For the tin-rich alloy, both convections go in the ccw direction. The streamlines, velocities, temperatures, mass fractions, and volume fractions of solid have been compared during and after solidification. An overall good agreement has been found between the two simulation results. However, the tendency toward segregated channel formation has been shown to be quite different: it is more pronounced for Pb-48 wt pct Sn when using FEM, while the opposite occurs for the Sn-5 wt pct Pb alloy. In the same way, the direction and the intensity of these channels are also quite different. Except for the remelted channel located at the boundaries of the cavity (top for lead-tin and bottom for tin-lead), the FVM formulation predicts low intensity inclined channels, which extend far from the boundaries. On the other hand, segregated channels predicted by FEM are horizontal, of higher intensity, and confined near the boundaries. This behavior is not yet fully understood, but several explanations have been proposed. The first one is associated with the handling of the boundary conditions, whereas a second possibility could be the discretization of the friction term in the momentum conservation equation. The FVM scheme does not express the no-slip condition at the boundaries by imposing a zero value of the tangential component of the velocity (as done in the FEM scheme), and a stress balance is applied instead. It appears that the velocity boundary layer is very thin near the boundary where the fluid arrives (top for Pb-48 wt pct Sn and bottom for Sn-5 wt pct Pb). A refined grid in these regions might be necessary. The tendency to form segregated channels is also more pronounced when the velocity of the fluid is higher. For example, v_{max} is higher with FVM as compared with FEM in the Sn-5 wt pct Pb alloy and the tendency to channel formation is also more pronounced. The reverse occurs for Pb-48 wt pct Sn. In both formulations, one can observe a possible correlation between the intensity of macrosegregation and the freckling tendency: a stronger relative segregation seems to lead to more channel patterns. Segregated channels originate from an instability, when the velocity of the interdendritic fluid becomes larger than the speed of the isotherms (in fact, these are the components along the thermal gradient). Since no instability criterion is built in both formulations, it is not

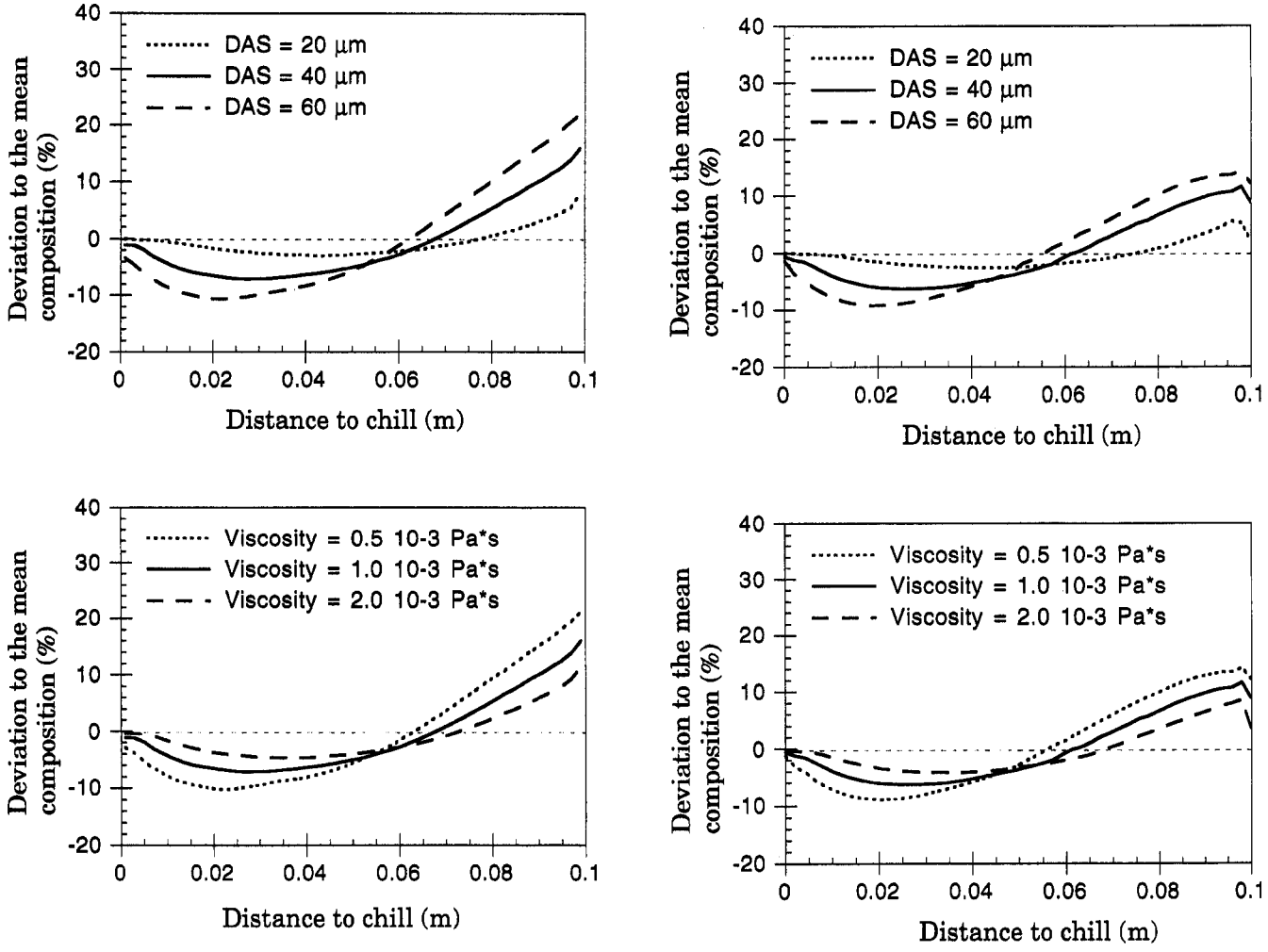

Fig. 9—Influence of the secondary DAS (top) and viscosity (bottom) on the relative tin mass fraction variations at the end of solidification. The profiles calculated at midheight of the cavity by FVM (left) and FEM (right) are plotted as a function of the distance to the chill.

surprising that the spacing or depth of these channels may be influenced by many numerical aspects (mesh size, time-step, *etc.*), including the formulation itself. The present test case is clearly a very good benchmark test for scientists doing macrosegregation calculations. The simulation results obtained with the FVM and FEM formulations have been compared very favorably with the experimental results of HH.

ACKNOWLEDGMENTS

This research, which is part of the Brite–Euram Program No. 1112, "A European Program on Aluminium Casting Technology", has been financed by the European Community (Brussels, Belgium), and by the Office Fédéral de l'Education et de la Science (Bern, Switzerland).

REFERENCES

1. D.J. Hebditch and J.D. Hunt: *Metall. Trans.*, 1974, vol. 5, pp. 1557-64.
2. V.R. Voller and S. Sundarraj: *Int. J. Heat Mass Transfer*, 1995, vol. 38, pp. 1009-18.
3. P. Nandapurkar, D.R. Poirier, J.C. Heinrich, and S. Felicelli: *Metall. Trans. B*, 1989, vol. 20B, pp. 711-21.
4. J.C. Heinrich, S. Felicelli, P. Nandapurkar, and D.R. Poirier: *Metall. Trans. B*, 1989, vol. 20B, pp. 883- 91.
5. W.D. Bennon and F.P. Incropera: *Int. J. Heat Mass Transfer*, 1987, vol. 30, pp. 2171-87.
6. J. Ni and C. Beckermann: *Metall. Trans. B*, 1991, vol. 22B, pp. 349-61.
7. S.N. Tewari and R. Shah: *Metall. Mater. Trans. A*, 1996, vol. 27A, pp. 1353-62.
8. K. Miyazawa and K. Schwerdtfeger: *Arch. Eisenhüttenwes.*, 1981, vol. 52, pp. 415.
9. G. Lesoult and S. Sella: in *Non Linear Phenomena in Materials Science*, G. Martin and L.P. Kubin, eds., Trans Tech Publications, Aedermannsdorf, Switzerland, 1988, pp. 167-78
10. C.Y. Wang and C. Beckermann: *Metall. Mater. Trans. A*, 1996, vol. 27A, pp. 2754-64, pp. 2765-83, and pp. 2784-95.
11. J. Jang and A. Hellawell: *Ironmaking and Steelmaking*, 1991, vol. 18, pp. 267-74.
12. J. Jang and A. Hellawell: *Ironmaking and Steelmaking*, 1991, vol. 18, pp. 275-83.
13. H. Kato and J.P. Cahoon: *Metall. Trans. A*, 1985, vol. 16A, pp. 579-87.
14. M. Schneider and C. Beckermann: *Int. J. Heat Mass Transfer*, 1995, vol. 38, pp. 3455-73.
15. E. Hang, A. Mo, and H.J. Tevik: *Int. J. Heat Mass Transfer*, 1995, vol. 38, pp. 1553-63.
16. H.W. Huang, J.C. Heinrich, and D.R. Poirier: *Model. Simul. Mater. Sci. Eng.*, 1996, vol. 4, pp. 245-59.
17. S.D. Felicelli, J.C. Heinrich, and D.R. Poirier: *Metall. Trans. B*, 1991, vol. 22B, pp. 847-59.
18. H. Combeau and G. Lesoult: *6th Conf. on Modeling of Casting, Welding and Advanced Solidification Processes*, Palm Coast, FL, T.S.

Piwonka, V. Voller, and L. Katgerman, eds., TMS, Warrendale PA, 1993, pp. 201-08.
19. P.J. Prescott and F.P. Incropera: *Metall. Trans. B*, 1991, vol. 22B, pp. 529-40.
20. W.D. Bennon and F.P. Incropera: *Num. Heat Transfer*, 1988, vol. 13, pp. 277-96.
21. I. Ohnaka: *Proc. Conf. "State of the Art of Computer Simulation of Casting and Solidification Processes,"* E-MRS 14, H. Fredriksson, ed., Les Editions de Physique, Les Ulis, France, 1986, pp. 211-23.
22. M. Rappaz and V. Voller: *Metall. Trans. A*, 1990, vol. 21A, pp. 749-53.
23. S. Ganesan and D.R. Poirier: *Metall. Trans. B*, 1990, vol. 21B, pp. 173-81.
24. D.R. Poirier, P.J. Nandapurkar, and S. Ganesan: *Metall. Trans. B*, 1991, vol. 22B, pp. 889-900.
25. C. Prakash and V. Voller: *Num. Heat Transfer*, 1989, part B, vol. 15, pp. 171-89.
26. H. Combeau, F. Roch, J.C. Chevrier, I. Poitrault, and G. Lesoult: *Advanced Methods in Heat Transfer*, Southampton, Great Britain, July 17 1990, L.C. Wrobel, ed., Springer-Verlag, New York, NY, 1990, vol. 3, pp. 79-90.
27. Q.Z. Diao and H.L. Tsai: *Metall. Trans. A*, 1993, vol. 24A, pp. 963-73.
28. X. Zeng and A. Faghri: *Num. Heat Transfer*, 1994, part B, vol. 25, pp. 467-80.
29. M. Reza Aboutalebi, M. Hassan, and R.I.L. Guthrie: *Metall. Mater. Trans. B*, 1995, vol. 26B, pp. 731-44.
30. D. Xu and Q. Li: *Num. Heat Transfer*, 1991, part A, vol. 20, pp. 181-201.
31. A. Mo, T. Rusten, H.J. Thevik, B.R. Henriksen, and E.K. Jensen: *126th TMS Annual Meeting*, Orlando, FL, 1997, TMS, Warrendale, PA, 1997, pp. 667-74.
32. S.K. Sinha, T. Sundarajan, and V.K. Garg: *Int. J. Heat Mass Transfer*, 1993, vol. 36, pp. 2349-58.
33. M.J.M. Krane and F.P. Incropera: *Metall. Mater. Trans. A*, 1995, vol. 26A, pp. 2329-40.
34. A. Mo: *Int. J. Heat Mass Transfer*, 1993, vol. 36, pp. 4335-40.
35. H.J. Thevik and A. Mo: *Int. J. Heat Mass Transfer*, 1997, vol. 40, pp. 2055-65.
36. D. Xu, Q. Li, and R.D. Pehlke: *AFS Trans.*, 1991, vol. 103, pp. 737-45.
37. H. Shahani, G. Amberg, and H. Fredriksson: *Metall. Trans. A*, 1992, vol. 23A, pp. 2301-11.
38. M.C. Flemings and G.E. Nereo: *Trans. TMS-AIME*, 1968, vol. 242, pp. 50-55.
39. I. Vannier, H. Combeau, and G. Lesoult: *Mater. Sci. Eng.*, 1993, vol. A173, pp. 317-21.
40. I. Vannier: Ph.D. Thesis, Institut National Polytechnique de Lorraine, Nancy, France, 1995.
41. P. Thévoz, M. Rappaz, and J.-L. Desbiolles: *Light Metals*, C.M. Bickert, ed. TMS, Warrendale, PA, pp. 975- 84.
42. N. Ahmad: Ph.D. Thesis No 1349, Ecole Polytechnique Fédérale de Lausanne, Lausanne, Switzerland, 1995.
43. A.E. Scheidegger: *The Physics of Flow through Porous Media*, 3rd ed., University of Toronto Press, Toronto, 1974, p. 141.
44. S.V. Patankar: *Numerical Heat Transfer and Fluid Flow*, Hemisphere, Washington, D.C., 1980.
45. J.P. Van Doormaal and G.D. Raithby: *Num. Heat Transfer*, 1984, vol. 7, pp. 147-63.
46. J.L. Desbiolles, M. Rappaz, J.J. Droux, and J. Rappaz: *Proc. E-MRS Conf.*, H. Fredriksson, ed., Les Editions de Physique, Paris, 1986, pp. 49-55.
47. H. Combeau, J.-M. Drezet, A. Mo, and M. Rappaz: *Metall. Mater. Trans. A*, 1996, vol. 27A, pp. 2314-27.
48. G. De Vahl Davis and I.P. Jones: *Int. J. Num. Methods in Fluids*, 1983, vol. 3, pp. 227-48.
49. A.N. Brooks and T.J.R. Hughes: *Comp. Meths. Appl. Mech. Eng.*, 1982, vol. 32, pp. 199-259.
50. F. Thomasset: *Implementation of Finite Element Methods for Navier–Stokes equations*, Springer-Verlag, New York, NY, 1981, p. 81.
51. H. Fredriksson and S.O. Nilsson: *Metall. Trans. B*, 1978, vol. 9B, pp. 111-20.
52. W. Kurz and D.J. Fischer: *Fundamentals of Solidification*, Trans Tech Publications, Aedermannsdorf, Switzerland, 1989.